



Low temperature activation of inert hexagonal boron nitride for metal deposition and single atom catalysis

Yu Lei ^{a,b,c,†}, Srimanta Pakhira ^{d,e,†}, Kazunori Fujisawa ^{a,b,c}, He Liu ^{b,c,f},
Cynthia Guerrero-Bermea ^g, Tianyi Zhang ^{b,c,h}, Archi Dasgupta ^f, Luis M. Martinez ⁱ,
Srinivasa Rao Singamaneni ⁱ, Ke Wang ^b, Jeff Shallenberger ^b, Ana Laura Elías ^{a,b,c,j},
Rodolfo Cruz-Silva ^k, Morinobu Endo ^k, Jose L. Mendoza-Cortes ^{l,*},
Mauricio Terrones ^{a,b,c,f,h,k,*}

^a Department of Physics, The Pennsylvania State University, University Park, PA 16802, USA

^b Materials Research Institute, The Pennsylvania State University, University Park, PA 16802, USA

^c Center for 2-Dimensional and Layered Materials, The Pennsylvania State University, University Park, PA 16802, USA

^d Department of Physics, Indian Institute of Technology Indore (IITI), Simrol Campus, Khandwa Road, Simrol, Indore, Madhya Pradesh 453552, India

^e Department of Metallurgy Engineering and Materials Science (MEMS) & Centre for Advanced Electronics (CAE), Indian Institute of Technology Indore (IITI), Simrol Campus, Khandwa Road, Simrol, Indore, Madhya Pradesh 453552, India

^f Department of Chemistry, The Pennsylvania State University, University Park, PA 16802, USA

^g Centro de Investigación Científica de Yucatán, A.C., Mérida, Yucatán 97205, Mexico

^h Department of Material Science and Engineering, The Pennsylvania State University, University Park, PA 16802, USA

ⁱ Department of Physics, The University of Texas at El Paso, El Paso, TX 79968, USA

^j Department of Physics, Binghamton University, Binghamton, NY 13902, USA

^k Research Initiative for Supra-Materials and Global Aqua Innovation Center, Shinshu University, 4-17-1Wakasato, Nagano 380-8553, Japan

^l Department of Chemical Engineering & Materials Science, Michigan State University, East Lansing, MI 48824, USA

Hexagonal boron nitride (hBN) has long been considered chemically inert due to its wide bandgap and robust covalent bonds. Its inertness hinders hBN from functionalization for energy conversion applications. A question arising is whether it is possible to make hBN chemically reactive. Here, we report cryomilling in liquid N₂, as an effective strategy to activate the chemical reactivity of hBN by engineering different vacancies to produce defective-BN (d-BN). The local reactivity of the vacancies is probed by photoluminescence (PL) emissions and electron spin resonance spectroscopy (ESR). Density functional theory calculations reveal that the formation of different vacancies with/without oxygen cause the creation of mid-gap states that are responsible for the PL emissions in the visible region. These vacancies also generate localized free radicals which are both theoretically and experimentally confirmed by spin density calculations and ESR. Due to the vacancy induced free radicals and Fermi level shifts, d-BN can be controllably functionalized with single metal atoms by the spontaneous reduction of metal cations; mono-metallic or bi-metallic clusters can also be effectively reduced. As a proof of concept, the surface-bound metal nanostructures, especially substrate confined single metal atoms, exhibit improved hydrogen evolution catalytic performance, and can be further used for sensing, and quantum information.

* Corresponding authors.

E-mail addresses: Mendoza-Cortes, J.L. (jmendoza@msu.edu), Terrones, M. (mut11@psu.edu).

† Y.L. and S.P. contributed equally in this article.

Keywords: Boron nitride (BN); Transition metal reduction; Defect engineering; Single atom catalysis; Density functional theory (DFT)

Introduction

Hexagonal boron nitride (hBN) is a structural analog of graphite, where alternating B/N atoms are covalently bonded into hexagonal layers, which are held together by weak van der Waals forces. The main distinction is that the B-N covalent bonds are polar and partially ionic due to the electronegativity difference between B and N [1]. Namely, graphene has evenly distributed π electrons, whereas hBN has a reduced electron-delocalization in the π bonds because the lone pair electrons in the p_z orbital of N atoms are more confined [2]. These unique structural properties in hBN result in electrical insulation, high thermal conductivity, excellent oxidation resistance, and hydrophobicity, which promotes various applications such as dielectric layers, anti-wear/corrosion coatings, and high-temperature crucibles [1,3–7]. However, its chemical inertness and mechanical robustness have made hBN functionalization difficult.

Defect engineering has emerged as a primary approach to tailor the physicochemical properties and further extend the functionalities of layered materials [8]. By introducing defects, some properties were observed such as defect states, bandgap reduction, and free radicals in hBN [7,9–18]. However, energy-demanding methods, such as plasma [19–22] and ball-milling [23,24], are needed to introduce defects and functional groups due to the hBN mechanical robustness. Ball-milling is a scalable approach to introduce defects in hBN, but the prolonged milling time (>20 h) may lead to unwanted contamination from the milling environment [25,26]. Accordingly, we hypothesized that ball-milling in a cryogenic environment (*i.e.* cryomilling in N_2 at 77 K) could be more selective in the generation of homogeneous defects because several undesirable side-reactions will be suppressed due to the low thermal energy available. We also inferred that this selectivity might help in energy efficiency, thus reducing the milling time. This technique, cryomilling, has been widely used to obtain fine-grained metallic nanostructures for improved mechanical properties [26]. During the conventional ball milling, the temperature usually rises with the milling time, which always leads to structure recrystallization and promote the side reaction with the milling media, such as oxidation when O_2 is presented. By maintaining the cryogenic environment, those side reactions can be significantly suppressed, which further shortened the milling time and lead to a finer grain structure [26]. Other than metallic nanostructure, due to its high strain rate deformation at cryogenic temperature, it has also been used to unzip carbon nanotubes into graphene [27], which shows its potential to break the covalent bonds and create defects in 2D materials.

Here, we show that defects can be introduced into bulk hBN by a scalable cryomilling process in a matter of minutes. Cryomilling takes advantage of conventional milling and cryogenic N_2 environment so that the milling time can be significantly reduced, and oxidation can be substantially suppressed. During cryomilling, hBN can be activated by the creation of vacancies with hydroxyl groups to produce defective-BN (d-BN). PL emissions within the visible region and electron spin resonance

(ESR) signals can be detected in d-BN, implying the changes in the band structure and the creation of free radicals. Subsequently, this d-BN is able to donate electrons to metal cations (Ag, Fe, Cu, Au, and Pt) to form into single atoms and sub-nanoclusters (2–8 nm in diameter) at room temperature (RT). To further understand this phenomenon, we turn to theoretical calculations which revealed that different types of vacancies present in d-BN significantly change the band structure and shifts of Fermi energy (E_F) higher than the reduction potential of the metal cations. The calculated spin density maps near the vacancies are well aligned with the ESR spectra that free radicals can be observed near the vacancies in d-BN. In essence, these vacancies are the reactive sites to reduce metal cations spontaneously on the d-BN surface, as well as the PL emission sites within the visible region. Due to the differences in diffusion barriers and adsorption energy, different metal species are formed into various size and morphologies, that single Pt atoms are confined at the vacancies, while Au, Ag, Fe, and Cu are formed into sub-nanoclusters. Atomically dispersed Pt atoms is a promising platform for single atom catalysis (SAC), while d-BN support may hinder the overall electron transport. To improve the electron transport, bi-metallic AgPt sub-nanocluster with atomically dispersed Pt atoms were reduced by d-BN (d-BN:AgPt). Electron donation from Ag to Pt is confirmed by both X-ray photoelectron spectroscopy (XPS) and density functional theory (DFT) calculations. The materials were then tested as the catalysts for the hydrogen evolution reaction (HER), and d-BN:AgPt shows excellent HER activity with a turnover frequency (TOF) of $10.17 H_2 s^{-1}$ at 100 mV overpotential when both Ag and Pt atoms are considered as the active sites, which is better than commercial Pt/C catalysts. This superior performance is attributed to the robust anchoring of atomically dispersed Pt atoms and the synergetic effects among AgPt and d-BN. Our results highlight how cryomilling can be used to nanoengineer defects in bulk hBN and to stabilize different metal nanostructures, including single atoms and mono/bi-metallic nanoclusters with broad applications in sensing, catalysis, quantum information and aerospace systems. This strategy can be applied to other metals and other layered materials, thus opening new horizons in the activation of inert materials.

Results and discussion

Boron nitride activation

Pristine hBN powders were subjected to cryomilling in liquid N_2 (77 K) to produce d-BN. The degree of defectiveness in d-BN is controlled by the cryomilling time. The main advantage of milling hBN at 77 K is the reduced milling time, due to the promotion of fracture and pulverization. Different d-BN samples with various cryomilling times (9, 18, 27, 45, 90, 120, 150, and 900 min) were prepared and named as 9BN, 18BN, 27BN, 45BN, 90BN, 120BN, 150BN, and 900BN, respectively. Structural pulverization and amorphization of hBN is commensurate with the cryomilling time [28] (Fig. 1a). X-ray diffraction (XRD) patterns further confirmed a gradual rise in disorder as the

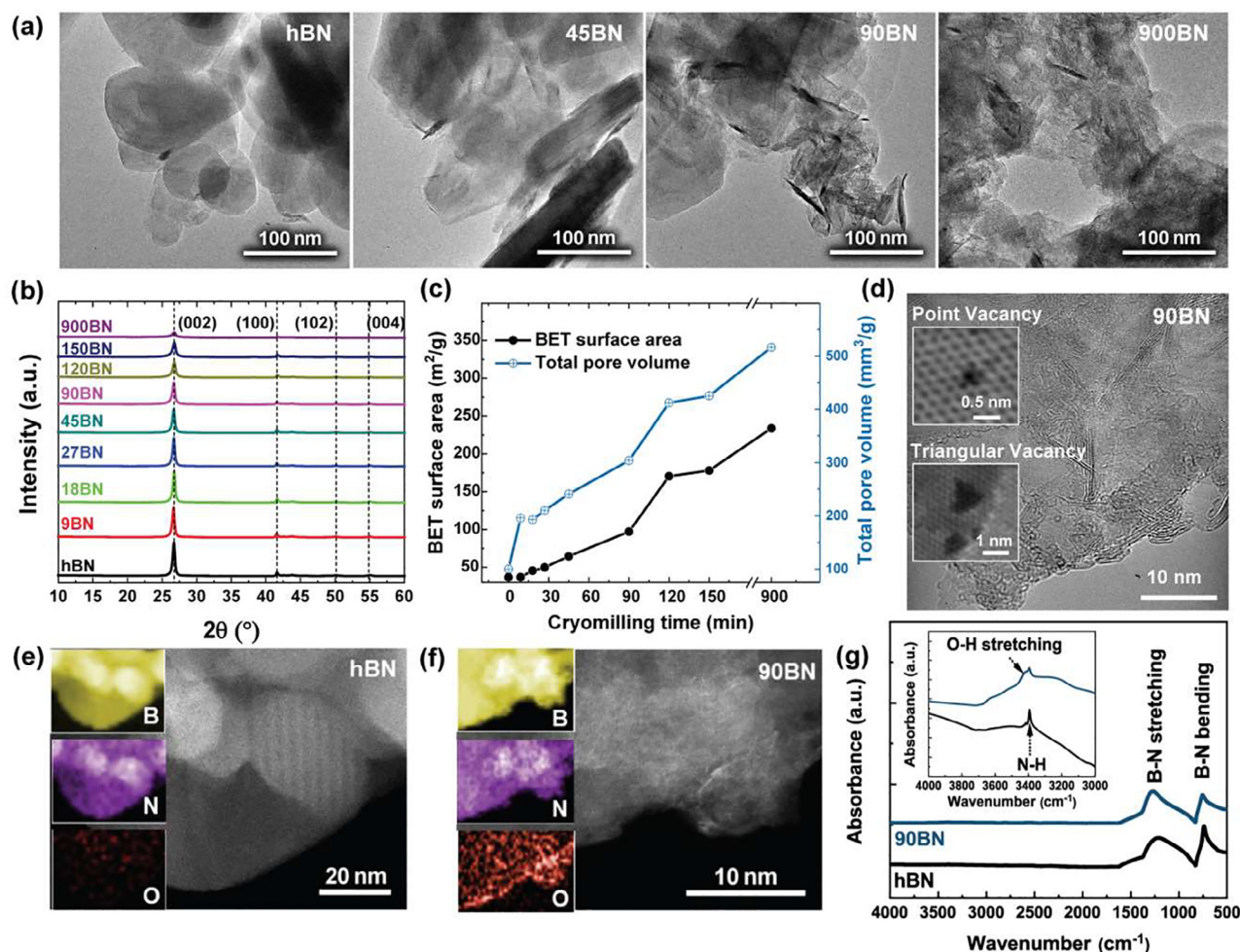


FIGURE 1

hBN activation via cryomilling: (a) TEM images of pristine hBN, 45BN, 90BN, and 900BN, which show BN platelets undergo deformation and amorphization with longer cryomilling time. (b) XRD spectra of hBN and d-BN taken at different cryomilling times, up to 900 min. (c) BET surface area and total pore volume values are directly correlated to cryomilling time. (d) Representative HR-TEM images of the 90BN show defective edges and amorphous-like regions; insets depict scanning transmission electron microscopy-annular dark-field (STEM-ADF) images of triangular and point vacancies. HAADF images of (e) hBN and (f) 90BN, show the corresponding EELS mappings of B, N, and O. (g) The FTIR spectra of hBN and 90BN, and the inset shows the zoom in of 4000–3000 cm^{-1} .

cryomilling time increases, as evidenced by the hBN (002) peak becoming weaker and broader (Fig. 1b). Longer cryomilling times result in a decrease of both the crystalline grain size (Fig. S1a) and the overall particle size (Fig. S1b), caused by the shearing force during milling. Thus, more surfaces and edges become exposed with longer cryomilling times, which significantly increase the surface area from 37 to 234 $\text{m}^2 \text{g}^{-1}$ (Fig. 1c). This was confirmed by N_2 adsorption isotherms of different d-BN materials (Fig. S2) and is consistent with shear exfoliation promoting the formation of small particles. High-resolution transmission electron microscopy (HRTEM) reveals defects in atomic scale, including triangular/point vacancies (Fig. 1d) and disordered structures with extended vacancies (Fig. S3). Due to the dangling bonds, the vacancies and edges are more favorable to adsorb heteroatoms from the milling media. In this case, hBN was loaded to the cell under the air. Thus, the oxygen (O) tends to be adsorbed during the milling process. Electron energy loss spectroscopy (EELS) mappings (Fig. 1e–f) reveal that more O can be found in 90BN

vs. hBN, especially at the edges. XPS indicates that the O content increases by $\sim 2 \text{ at.}\%$ on the surface of 90BN when compared to pristine hBN. The O was also probed by FTIR (Fig. 1g), that a broad shoulder at 3419 cm^{-1} emerged as cryomilling time increased, indicating the formation of hydroxyl groups bonded with BN (BN-OH) in 90BN [5].

Due to the similarity in the atomic number (Z) contrast between B and N, the directly identification of the types of vacancies in bulk d-BN samples by STEM is challenging. Temperature dependent X-band ESR was then carried out with frequency = 9.43 GHz (Fig. 2a), to identify the presence of paramagnetic defects in d-BN by detecting the unpaired electrons near the vacancies. Defect-free hBN should not show any ESR-active features due to its intrinsic diamagnetism [29]. However, in practice, the starting hBN was found to be B-rich (Fig. S4), which is consistent with previous studies [30]. It results in small ESR signals found in pristine hBN (Fig. S5) with a g value of about 2.0021 (resonance field 3351 G) when the measurements were carried out at room

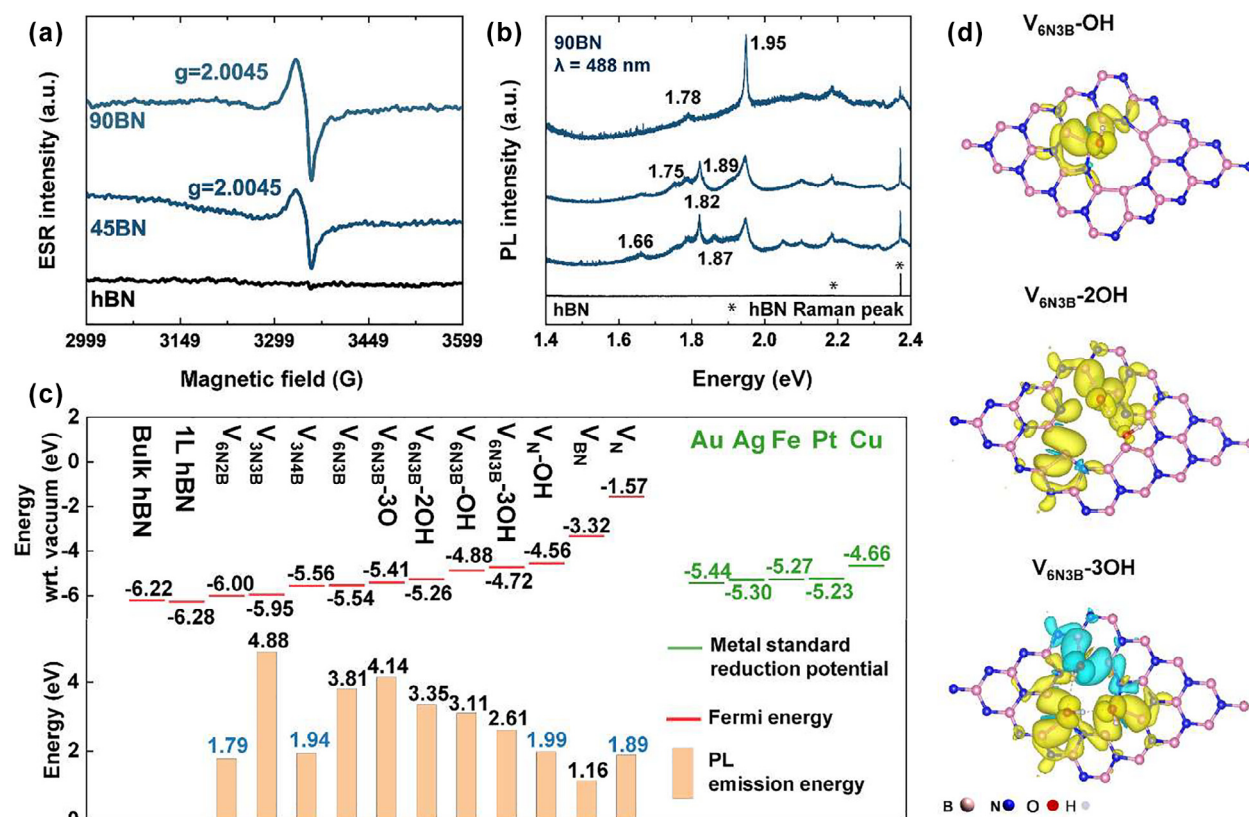


FIGURE 2

hBN activation mechanism. (a) ESR spectra obtained at 60 K for hBN, 45BN, and 90BN. (b) Room-temperature PL spectra of 90BN and hBN with a 488 nm excitation laser. (c) Top: A band alignment diagram with respect to vacuum for pristine hBN (bulk-, monolayer), and with defects (V_N , V_N-OH , V_{BN} , V_{3N3B} , V_{3N4B} , V_{6N2B} , V_{6N3B} , $V_{6N3B-OH}$, $V_{6N3B-2OH}$, $V_{6N3B-3OH}$, $V_{6N3B-3O}$) as well as Ag^+/Ag^0 , Pt^{4+}/Pt^{2+} , Au^{3+}/Au^0 , Cu^{2+}/Cu^+ , and Fe^{3+}/Fe^{2+} standard reduction potentials (green lines). The red lines indicate the Fermi energy; Bottom: Calculated PL emissions due to the listed defects above. (d) Selected spin density maps created for $V_{6N3B-OH}$, $V_{6N3B-2OH}$, and $V_{6N3B-3OH}$.

temperature (293 K). The peak intensity is commensurate with the cryomilling time as shown by ESR measurements of 45 and 90BN d-BN samples performed at 60 K, which reveals an intense ESR signal with a g value of 2.0045 and a peak-to-peak line width (ΔH_{pp}) of 26 G. These ESR features are consistent with the existence of an unpaired electron localized at the nitrogen-vacancy sites (boron-rich vacancies) [29]. In other words, more nitrogen vacancies were produced with longer cryomilling times, as shown by the signal intensity being directly proportional to spin concentration. Furthermore, these introduced vacancies are also responsible of defect-induced levels between the valence and conduction bands of hBN, giving rise to various photon emissions ranging from 1.56 to 2.1 eV (Figs. 2b and S6). Among those, emissions at 1.66, 1.75, 1.78, 1.82, 1.87, 1.89, and 1.95 eV are commonly found with the occurrence above 60 % (Fig. S6). Previous studies have indicated that the PL emissions in the visible region from hBN is due to the formation of structural vacancies, which means that the vacancies could serve as the single photon emitters [15].

In order to elucidate the roles of vacancies in d-BN, first principles calculations were performed at the level of unrestricted hybrid density functional theory (UDFT) with dispersion corrections; UDFT/B3LYP-D2 (or DFT for short) [31,32–35]. As a scal-

able process to create defects in bulk hBN, cryomilling tends to create various types of defects. XPS analysis (Fig. S4b), ESR (Fig. 2a) signals, and FTIR results (Fig. 1g) indicate that the majority of the defects are B-rich vacancies (N vacancies) with OH groups. Thus, various possible defects in the d-BN have been investigated by developing 11 model systems (Fig. S7). Each defect is named differently where the sub-index indicates the atom missing while the hyphen is to show the terminal group in the defect, e.g. V_N , V_N-OH , V_{BN} , V_{3N3B} , V_{3N4B} , V_{6N2B} , V_{6N3B} , $V_{6N3B-OH}$, $V_{6N3B-2OH}$, $V_{6N3B-3OH}$, $V_{6N3B-3O}$. The results indicate that each defect modifies the electronic properties differently (Table S1). The Fermi energy (E_F) is upward shifted by the listed defects (Fig. 2c, up). For instance, by creating a single nitrogen vacancy into BN (V_N), the E_F shifts to -1.57 eV, which is well above the reduction potentials of metal ions, including Ag^+/Ag (-5.30 eV), Pt^{4+}/Pt^{2+} (-5.23 eV), Au^{3+}/Au^0 (-5.44 eV), Cu^{2+}/Cu^+ (-4.66 eV), and Fe^{3+}/Fe^{2+} (-5.27 eV). Other than V_N , the other defects show a similar trend, which suggests that they can serve as the reactive sites to transfer electrons to selected metal ions for the reduction reaction. In addition, the band gaps (E_g) of various theoretical d-BN can vary from 1.16 to 4.88 eV. These values are close to the experimental PL data (Fig. 2b), which suggest the identification of the defect types. More

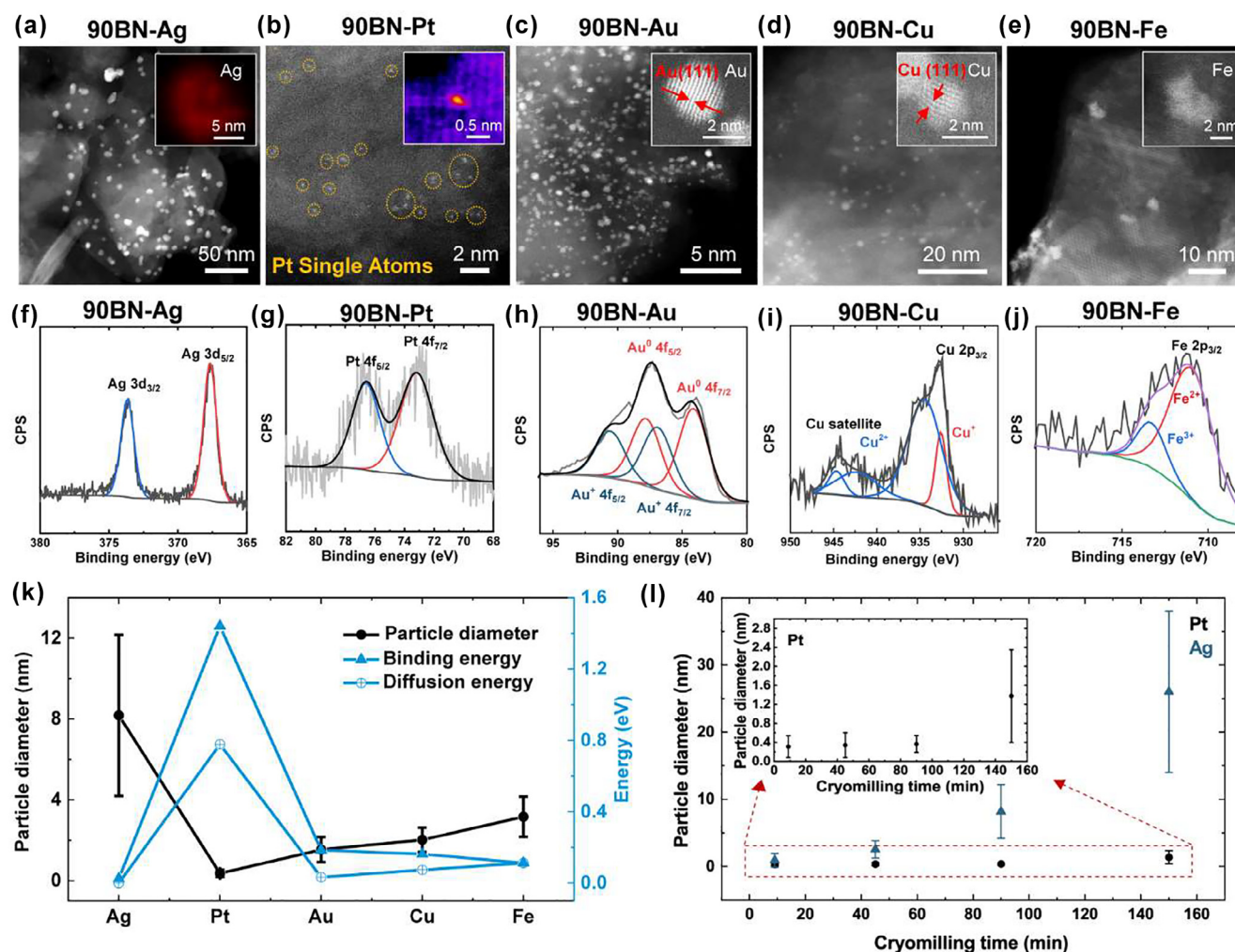


FIGURE 3

Metal reduction by d-BN. STEM/EDX and XPS characterization of (a, f) 90BN-Ag, (b, g) 90BN-Pt, (c, h) 90BN-Au, (d, i) 90BN-Cu and (e, j) 90BN-Fe. (k) Summary of metal diameters obtained from the STEM images, and the relation with the reported metal diffusion barriers and binding energies on hBN⁴⁰. (l) Comparison of metal diameters for Ag and Pt on 9BN, 45BN, 90BN, and 150BN, inset is the zoomed in region for Pt diameters.

specifically, the electronic band gaps of V_N , $V_N\text{-OH}$, V_{3N3B} and V_{6N2B} agree well with the some of the experimental PL peaks (Fig. 2c, bottom). On the other hand, V_{3N3B} , $V_{6N3B}\text{-OH}$, $V_{6N3B}\text{-2OH}$, $V_{6N3B}\text{-3OH}$ and $V_{6N3B}\text{-3O}$ exhibit intra-band transitions which matches with other experimental PL peaks (Fig. S6, Table S1). Therefore, the combination of PL measurements and quantum calculations have identified the defects present in the d-BN. Moreover, the electron spin densities of these various d-BN were also computed (Figs. 2d and S8). The spin density calculates the differences of spin up (α) and spin down (β). In other words, this is another way to estimate the presence of unpaired electrons. In the B-rich triangular vacancy terminated with OH groups ($V_{6N3B}\text{-OH}$, $V_{6N3B}\text{-2OH}$, and $V_{6N3B}\text{-3OH}$), electron spin density distribution was observed around the defect which indicates the existence of free radicals (Fig. 2d). This is a similar behavior for other defects that have been identified on this system (Fig. S8). Therefore, the spin density analysis explains the detected unpaired electrons by ESR in d-BN (Fig. 2a). It also reveals the mechanism of how the identified vacancies are able

to reduce the metal ions, which is by having available unpaired electrons that can be transferred when enough potential energy is available (Fig. 2c).

Metal reduction

Experimentally, different d-BNs samples were mixed with different aqueous solutions of metal precursors to reduce different metals into single atom and/or nanoclusters (Fig. 3). In particular, 9BN, 90BN, and 150BN samples were mixed with AgNO_3 , PtCl_4 , FeCl_3 , CuSO_4 , and HAuCl_4 to obtain Ag, Pt, Fe, Cu, and Au, respectively. More specifically, when d-BNs were added into the AgNO_3 aqueous solution, the color changed from white to dark gray indicating the reduction of Ag (Fig. S9a). It is worth noting that the reactivity towards reducing Ag^+ is directly related to the cryomilling time, since more Ag is reduced when using 150BN than with 9BN. This is consistent with the proposed reduction mechanism because more cryomilling time generates more defects which increase the reducing power of d-BN towards

Ag⁺. XRD patterns show further evidence that Ag reduction is correlated to the presence of cryomilling induced defects; *i.e.* the Ag (111) peak emerges and increases directly proportional to cryomilling time (Fig. S10). A similar trend was observed when the metal precursor was changed to PtCl₄ (Fig. S9b, inset). UV-Vis spectroscopy confirms the shifts to shorter wavelength (*i.e.* hypsochromic) in adsorption maxima when comparing 90BN and 150BN with 9BN, indicating that more [PtCl₆]²⁻ ions are reduced and immobilized on 90BN and 150BN (Fig. S9b) [36]. Similar trends are observed for reductions of Au, Cu, and Fe (Fig. S9c–e). STEM images and the Ag energy-dispersive X-ray spectroscopy (EDX) mapping reveal that Ag nanoparticles have an averaged diameter of 8.2 nm in 90BN, which is consistent with a nanocluster being formed (Fig. 3a). For the Pt case, the size distribution analysis in 90BN-Pt reveals that most of the isolated atoms (Fig. 3b). The Pt single atoms are also confirmed by extended X-ray absorption fine structure (EXAFS) spectra at the Pt L₃-edge of 90BN-Pt as shown in Fig. S11a; as well as from Pt foil and PtO₂, which are the references for Pt-Pt and Pt-O bonds, respectively. The Fourier transform spectra exhibits one prominent broad peak centered at ~1.7 Å for 90BN-Pt (Fig. S11a). The Pt-Pt bonding length obtained from Pt foil is ~2.55 Å, which is clearly larger than that obtained for our electrocatalyst samples. In addition, when compared to PtO₂, no second-shell Pt-Pt peak at ~3 Å can be observed in 90BN-Pt, thus confirming the presence of atomically dispersed Pt in 90BN-Pt. Similarly, for Au, Cu, and Fe reduction; nanoclusters were formed with diameters ranging from 2 to 4 nm, which were identified by STEM (Fig. 3c–e). The XPS peaks show that ions have been reduced, *i.e.* the Ag 3d, Pt 4f, Au 4f, Cu 2p, and Fe 2p electrons for 90BN-Ag, 90BN-Pt, 90BN-Au, 90BN-Cu, and 90BN-Fe, respectively (Fig. 3f–j). The binding energy of the Ag 3d_{5/2} peak is at 368.2 eV indicating the reduction of Ag⁺ into metallic Ag⁰ by 90BN (Fig. 3f) [37]. Unlike Ag, the peak for Pt 4f_{7/2} is at 73.20 eV (Fig. 3g), which is ~3 eV higher than those of bulk Pt. The positive chemical shift for 90BN-Pt relative to bulk Pt is caused by the formation of isolated Pt atoms as seen in Fig. 3b [38,39]. In 90BN-Au (Fig. 3h), the lower binding energy Au 4f_{7/2} peak (84.35 eV) was consistent with metallic gold, and a second Au 4f_{7/2} peak at 86.9 eV can be assigned to Au⁺, indicating the reduction of Au³⁺ to Au⁰ and Au⁺ by 90BN. Similar reduction can also be found in Cu and Fe (Fig. 3i–j). In addition, XPS analysis (Fig. S12) reveals that the metal loadings (Ag, Pt, Au, Cu, Fe) are 0.24, 0.05, 0.5, 1.0, and 0.2 at.%, respectively. Though the metal reductions are thermodynamically favorable for all the tested metals (Ag, Pt, Au, Cu, Fe), the disparity in the morphologies could be related to the BN-metal binding energies and kinetic barriers of metals on hBN [40], as well as the defect density in d-BN. As seen in Fig. 3k, Ag has the minimum diffusion barrier and binding energy, thus, small Ag clusters have the tendency to migrate and coalesce into larger nanoparticles, which has also been observed for other oxides [41,42] and chalcogenide [43] surfaces. On the contrary, Pt has the highest diffusion barrier and binding energy, which limits the Pt migration confining the Pt atoms within the vacancy sites after nucleation. As a result, Pt atoms are atomically dispersed on d-BN, rather than forming into nanoclusters or nanoparticles. For Fe, Au, and Cu, the diffusion barriers and binding energies are moderate, resulting in the for-

mation of nanoclusters with diameters ranging from 2 to 4 nm (Fig. 3k). The particle size and morphologies are also related to the defect density in d-BN. Fig. 3l summarized the metal particle sizes of Ag and Pt which were reduced with d-BN at different cryomilling times (9, 45, 90, and 150 min). It is clear that both Ag and Pt particle diameters are commensurate with the cryomilling time, but most of the Pt still remains in single atoms when the BN cryomilling time is less than 90 min. By increasing the cryomilling time, the distance between defects is significantly shortened, thus facilitate the metal diffusion and aggregation, resulting in larger metal particles.

Electrocatalytic activities

On the basis of the aforementioned analysis, d-BN offers a unique platform to reduce and stabilize nanoclusters, and even single atoms with the potential towards catalysis, and even SAC. In recent years, Pt-free [44–47] and Pt based SACs [48–52] for hydrogen evolution reaction (HER) has gained extensive attention. As a proof of concept, d-BN with atomically dispersed Pt atoms were used as the catalyst for HER. In order to improve the electrical conductivity, bi-metallic AgPt nanoclusters with different Ag:Pt ratios (90BN-Ag₂Pt₁, 90BN-Ag₁Pt₁, and 90BN-Ag₁Pt₂) were synthesized on d-BN by using Ag and Pt precursors. In 90BN-Ag₁Pt₁, the Ag and Pt atoms can be distinguished by Z-contrast in STEM-ADF images with atomic resolution, *i.e.* Pt (Z = 78) atoms are brighter than Ag (Z = 47) atoms (Fig. 4a–c). The image shows that Pt atoms are atomically dispersed within the Ag-Pt clusters (Fig. 4c). Similar to 90BN-Pt, the absence of the second-shell Pt-Pt peak and the lack of first-shell Pt-Pt bond when compared to Pt foil confirms the presence of atomically dispersed Pt in 90BN-Ag₁Pt₁ as well. However, due to the similarities in scattering strength among B, N, and O, it remains a challenge to distinguish Pt–O, Pt–B, and Pt–N bonds by studying the Pt L₃-edge EXAFS spectra [53].

The HER performance of d-BN with different metal particles: d-BN:Pt, d-BN:Ag and d-BN:AgPt (Ag₁Pt₂, Ag₁Pt₁, and Ag₁Pt₂) as well as Pt/C, was investigated in 0.5 M H₂SO₄ solutions (Fig. 4d–g). To improve the kinetic transport, we mixed the BN related samples with conducting carbon and Nafion (see Method in Supporting Information). Since the metals are mainly decorated on the surface of BN, the network formed by the conducting carbon and Nafion can efficiently transfer both electron and proton through the interface to the outer circuit. The as-prepared 90BN and 90BN-Ag electrodes exhibit negligible HER performance when compared to electrodes with Pt (90BN-Pt, 90BN-AgPt series, and the Pt/C), indicating that only the catalysts that contain Pt atoms are highly active (Fig. 4d). Among the electrodes with atomically dispersed Pt atoms, HER performances vary with the Ag to Pt molar ratio. In order to precisely count the Pt atoms in d-BN:Pt and d-BN:AgPt, proton-induced X-ray emission (PIXE) was utilized, as this is a non-destructive and sensitive approach to detect elements at the trace level. According to the PIXE analysis, any significant amount of contaminants could be detected in the studied samples, and the Ag to Pt molar ratio in the resultant hybrid compound with d-BN is close to that of the precursor (Table S2). The onset potential (over potential at 10 mA cm⁻²), Tafel slope, turnover frequency (TOF), and exchange current are summarized and compared to other

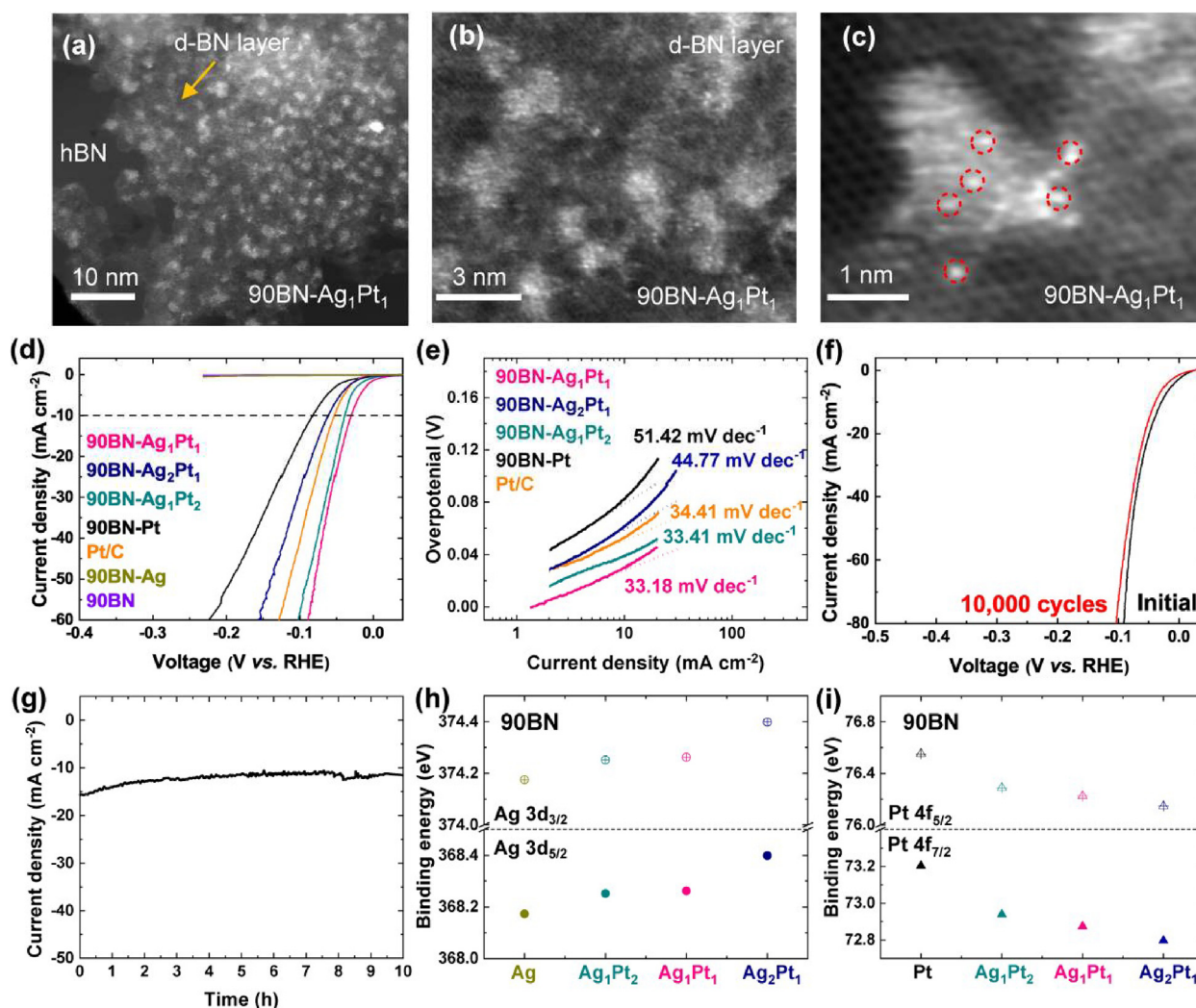


FIGURE 4

Characterization of AgPt bi-metallic sub-nanoclusters on d-BN and their HER performance. Representative 90BN-Ag₁Pt₁ STEM-ADF images at (a) low and (b, c) high magnifications, where the atomically dispersed Pt atoms in the Ag-Pt cluster are highlighted with red dashed circles. (d) HER polarization curves and (e) Tafel plots of 90BN with Ag, Pt, Ag₁Pt₁, Ag₁Pt₂, Ag₂Pt₁ are compared to Pt/C. (f) Durability measurements of the 90BN-Ag₁Pt₁, where the polarization curves were recorded at the 1st cycle, and after 10,000 cycles; (g) The amperometric *I*-*t* stability curve at a constant overpotential of 35 mV for 10 h. XPS for (h) Ag 3d_{3/2}/Ag 3d_{5/2} and (i) Pt 4f_{7/2}/Pt 4f_{5/2} peaks measured at different Ag-Pt compositions.

reported state-of-the-art Pt-based catalysts (Table S3) [54–56]. For 90BN-Pt, the onset potential (over potential at 10 mA cm⁻²) is 82 mV with a Tafel slope of 51 mV dec⁻¹ (Fig. 4d). The HER on the Pt surface undergoes the Volmer-Tafel reaction where the rate-limiting step is often the recombination step [57]. However, in 90BN-Pt, given that single Pt atoms are isolated within the inert hBN, the recombination of chemisorbed hydrogen atoms becomes sluggish, resulting in a relatively higher Tafel slope for 90BN-Pt when compared to that of Pt/C. Interestingly, the HER performance can be significantly improved by forming bimetallic Ag-Pt sub-nanoclusters. The best HER performance was achieved when the Ag to Pt molar ratio is 1 (90BN-Ag₁Pt₁); this electrode features an onset potential (over potential at 10 mA cm⁻²) of 30 mV and a Tafel slope of 33 mV dec⁻¹. The TOF of 90BN-Ag₁Pt₁ is ~194 times higher than that of Pt/C @ 100 mV (Table S3) when only Pt atoms are considered as the active sites.

The exchange currents obtained from 90BN-Ag₁Pt₁ are 4.4 times higher than that of Pt/C (Table S3) [56,58]. Since the Pt atoms are atomically dispersed on the support, the electrochemical active surface area (ECSA), which is proportional to the double-layer capacitance (*C*_{dl}), was used to compare the Pt active site density (Fig. S13a–e). Though 90BN-Ag₁Pt₂ has the highest Pt content based on PIXE results (Table S2), the *C*_{dl} of 90BN-Ag₁Pt₂ is 5.095 mF cm⁻², which is smaller than that of 90BN-Ag₁Pt₁ (5.795 mF cm⁻²). This indicates that the excess of Pt atoms is not exposed on the surface, and results in a decrease of the exchange current (0.65 mA cm⁻²) in 90BN-Ag₁Pt₂ when compared to that of 90BN-Ag₁Pt₁ (Table S3). Furthermore, the lifetime of the best performing catalyst 90BN-Ag₁Pt₁ was evaluated, and surprisingly after 10,000 cycles, the performance is comparable to that of the 1st cycle (Fig. 4f). Moreover, the amperometric current–time stability curve shows that the 90BN-Ag₁Pt₁ is stable

and robust by maintaining $\sim 10 \text{ mA cm}^{-2}$ without significant current loss for 10 h (Fig. 4g), and $\sim 20 \text{ mA cm}^{-2}$ for 50 h (Fig. S14a). No obvious morphology change (Fig. S14b) can be found in the STEM image of 90BN-Ag₁Pt₁ after the 50 h stability test, which further indicates the stability of our hBN materials. The long-term stability further confirms the confinement of the metals within d-BN regions while the surrounding inert hBN significantly limits the metal migration.

Electrochemical impedance spectroscopy (EIS) was used to evaluate the charge transfer resistance among the electrodes and a Randle circuit was used to model the electrochemical reaction near the surface (Fig. S13f). The fitting results show that the charge transfer resistance (R_p) is reduced by forming bimetallic AgPt clusters compared to 90BN-Pt (Table S4), indicating a faster Faradaic process at the catalyst/electrolyte interface when forming Ag-Pt clusters.

XPS analysis was used to investigate the electron transfer between Ag and Pt (Fig. 4h-i and S15). The spin-orbit splitting of Pt 4f was found to be 3.35 eV (Fig. S15a), and that of Ag 3d is about 6 eV (Fig. S15b). The peak positions of Pt 4f and Ag 3d are summarized in Fig. 4h-i. The binding energies of Pt 4f shift to a lower value as the Ag concentration increases, while binding energies of Ag 3d shift to higher values (Fig. 4h-i). The negative shifts in the Pt binding energy indicate that the Ag atoms donate electrons to the Pt atoms [59,60].

To further understand charge transfer between Ag and Pt in d-BN; the equilibrium structures, electronic band structures and Density of States (DOS) were calculated for d-BN:Pt and d-BN:Ag₁Pt₁ (Figs. S16-S17a). The DFT calculations showed that Pt and Ag₁Pt₁ adsorption on the d-BN surfaces is favorable as the formation energy (ΔE) of both systems are -2.57 eV and -2.89 eV , respectively, and their electronic properties indicate that the bandgap is reduced (Table S5). The electronic properties of the d-BN:Ag₂Pt₂ system were also computed by increasing the Ag and Pt atoms cluster size (Fig. S18a-b). Its formation was found to be also favorable with $\Delta E = -2.72 \text{ eV}$ (Table S5). The *d*-subshells contributions of Pt atoms in the total DOS were calculated for d-BN:Pt (Fig. S16) and d-BN:Ag₁Pt₁ (Fig. S17a), showing that the major contributing component is the *d*-subshells from the Pt. However, for d-BN:Ag₁Pt₁, a small contribution of the Ag 5s-subshell is observed around the E_F (Fig. S17a). Another configuration that is consistent with the experimental measurements is when the Ag₁Pt₁ is bonded through an O bond to the d-BN surface (Fig. S18c-d), however the results do not differ from the previous configuration.

To explain the HER mechanism of d-BN:Ag₁Pt₁, the reaction pathways for the d-BN:Pt, d-BN:Ag₁Pt₁, and d-BN:Ag₂Pt₂ were considered as: (i) cluster formation on d-BN; (ii) H^+ absorption on the metal cluster followed by reduction, *i.e.* $\text{H}^+ + \text{e}^- \rightarrow \text{H}_{\text{ad}}$; and (iii) H_2 formation, known as the Volmer-Tafel reaction, *i.e.* $2\text{H}_{\text{ad}} \rightarrow \text{H}_2$ and the Volmer-Heyrovsky reaction. The potential energy surface of the reaction pathway, with the free energy (ΔG) in the solvent (H_2SO_4) were calculated for d-BN:Pt, d-BN:Ag₁Pt₁ and d-BN:Ag₂Pt₂ (Figs. S19, S17b, and S20, respectively). The rate determinant step of the HER is the Volmer-Heyrovsky reaction when the H_2 molecule is formed. The barrier for d-BN:Pt ($\Delta G_{\text{H}^*} = 7.8 \text{ kcal mol}^{-1}$), is larger than for either d-BN:Ag₁Pt₁ ($\Delta G_{\text{H}^*} = 2.26 \text{ kcal mol}^{-1}$) or d-BN:Ag₂Pt₂ ($\Delta G_{\text{H}^*} = 3.44 \text{ kcal mol}^{-1}$),

which shows better HER catalytic activity for d-BN:Ag₁Pt₁ and d-BN:Ag₂Pt₂.

While electrocatalysis is a proof-of-concept application, these experimental insights into the selective reduction of metal ions on activated BN are universal to create stabilized single metal atoms and mono- or bi-metallic nanoclusters, that can be used for other emerging applications, *e.g.*, other catalysts, such as N_2 fixation [61], and virus/DNA sensing [62].

Conclusion

We demonstrate that vacancy engineering *via* cryomilling offers an effective and scalable approach to activate inert hBN powders. We have identified the reduction mechanism of the metals and characterized the different vacancies present in d-BN by both experimental and computational approaches. Using first-principles calculations, we have elucidated the mechanisms whereby specific vacancies in d-BN serve as the PL emission centers and the reactive sites for metal reductions. Combining this experimental-theory approach: we have demonstrated that d-BN reduces and deposits various metals, including Fe, Cu, Au, Ag, and Pt, into single atoms or nanoclusters. The latter particles could serve as stable catalysts or sensing sites for biomolecules. Additionally, d-BN:AgPt sub-nanoclusters containing atomically dispersed Pt atoms showed the best HER activity in acidic solutions, with a TOF of $10.17 \text{ H}_2 \text{ s}^{-1}$ at 100 mV overpotential when both Ag and Pt atoms are considered as the active sites. Our results pave a new way to activate hBN, which is long considered to be inert, *via* cryomilling. Cryomilling constitutes a reliable general method to introduce vacancies in bulk layered materials or bulk ceramics, which can reduce different metal atoms for catalysis, sensing, quantum information, and aerospace applications.

Materials and methods

Detailed materials and methods can be found in the [supplementary information](#).

Data availability

The data that support the plots within this paper and other findings of this study are available from the corresponding author upon reasonable request.

Declaration of Competing Interest

The authors declare that they have no known competing financial interests or personal relationships that could have appeared to influence the work reported in this paper.

Acknowledgements

The authors would like to acknowledge the support of the material characterization laboratory (MCL) at the Pennsylvania State University for providing characterization resources. The authors would also acknowledge the support of Aichi Synchrotron Radiation Center for EXAFS measurements. S.P. acknowledges the support from Science & Engineering Research Board-Department of Science and Technology (SERB-DST), Govt. of India for the Ramanujan Faculty Fellowship (Grant No. SB/S2/RJN-067/2017) and Early Career Research Award (ECRA, Grant No.

ECR/2018/000255). S.R.S and L.M.M acknowledge the financial support of University of Texas at El Paso, through startup funds. S.R.S also acknowledges American Chemical Society (ACS) Petroleum Research Funds (PRF) PRF# 59611-UNI10. L.M.M. thanks the National Science Foundation for the NSF-LSAMP Ph.D. fellowship. †Y.L. and S.P. contributed equally to this article.

Author contributions

Y. L., S. P., J.L. M.-C., and M. T. conceived the idea. Y. L. conducted most material synthesis and characterization analysis. S. P. performed the theoretical calculations and analysis. K. F. and K. W. performed TEM characterization and analysis. H. L. and C. G. helped with the material synthesis. H. L. and T. Z. also carried out the PL measurements. A. D. and H. L. carried out the adsorption measurements and analysis. L.M. M. and S.R. S helped with ESR measurements. J. S, R. C., and M. E. helped with the XPS measurements. A.L. E. discussed the results and helped prepare the figures. J.L. M.-C., and M. T. supervised the project and directed the research. Y. L., S. P., J.L. M., and M. T. interpreted the results and wrote the manuscript with feedback from the other authors. Y. L. and S. P. contributed equally.

Appendix A. Supplementary data

Supplementary data to this article can be found online at <https://doi.org/10.1016/j.mattod.2021.09.017>.

References

- [1] A. Pakdel et al., *Acta Mater.* 61 (4) (2013) 1266.
- [2] Q. Weng et al., *Chem. Soc. Rev.* 45 (14) (2016) 3989.
- [3] A. Pakdel et al., *Chem. Soc. Rev.* 43 (3) (2014) 934.
- [4] W.W. Lei et al., *Nat. Commun.* 6 (2015) 8.
- [5] Z.H. Cui et al., *Small* 10 (12) (2014) 2352.
- [6] E.J. Hamilton et al., *Science* 260 (5108) (1993) 659.
- [7] I. Jo et al., *Nano Lett.* 13 (2) (2013) 550.
- [8] Z. Lin et al., *2D Mater.* 3 (2) (2016) 022002.
- [9] K. Uosaki et al., *J. Am. Chem. Soc.* 136 (18) (2014) 6542.
- [10] Z. Liu et al., *ACS Nano* 13 (2) (2019) 1394.
- [11] Y. Lin et al., *J. Phys. Chem. C* 114 (41) (2010) 17434.
- [12] K. Uosaki et al., *Sci. Rep.* 6 (2016) 32217.
- [13] A. Guha et al., *ACS Catal.* 8 (7) (2018) 6636.
- [14] T.T. Tran et al., *Nat. Nanotechnol.* 11 (1) (2016) 37.
- [15] T.T. Tran et al., *ACS Nano* 10 (8) (2016) 7331.
- [16] D. Xu et al., *J. Phys. Chem. C* 118 (17) (2014) 8868.
- [17] Q.H. Weng et al., *Adv. Mater.* 29 (2017) 28.
- [18] M. Terrones et al., *Nano Lett.* 8 (4) (2008) 1026.
- [19] T. Ikuno et al., *Solid State Commun.* 142 (11) (2007) 643.
- [20] O.L. Krivanek et al., *Nature* 464 (7288) (2010) 571.
- [21] A. Pakdel et al., *ACS Nano* 8 (10) (2014) 10631.
- [22] R. Sevak Singh et al., *Appl. Phys. Lett.* 104 (16) (2014) 163101.
- [23] D. Lee et al., *Nano Lett.* 15 (2) (2015) 1238.
- [24] W. Lei et al., *Nat. Commun.* 6 (1) (2015) 1.
- [25] C.S. Tiwary et al., *Metall. Mater. Trans. A* 44 (4) (2013) 1917.
- [26] D. Witkin, E.J. Lavernia, *Prog. Mater. Sci.* 51 (1) (2006) 1.
- [27] C.S. Tiwary et al., *Carbon* 89 (2015) 217.
- [28] J.Y. Huang et al., *J. Am. Ceram. Soc.* 83 (2) (2000) 403.
- [29] T. Kolodiazny, D. Golberg, *Chem. Phys. Lett.* 413 (1–3) (2005) 47.
- [30] G. Postole et al., *Thermochim. Acta* 434 (1–2) (2005) 150.
- [31] A.D. Becke, *J. Chem. Phys.* 96 (3) (1992) 2155.
- [32] R. Dovesi et al., *Int. J. Quantum Chem.* 114 (19) (2014) 1287.
- [33] S. Grimme, *J. Comput. Chem.* 27 (15) (2006) 1787.
- [34] C. Lee et al., *Phys. Rev. B* 37 (2) (1988) 785.
- [35] S. Pakhira et al., *J. Phys. Chem. C* 121 (39) (2017) 21160.
- [36] P.-H. van Wyk et al., *Anal. Chim. Acta* 704 (1–2) (2011) 154.
- [37] NIST X-ray Photoelectron Spectroscopy Database, N. S. R. D. N., National Institute of Standards and Technology, Gaithersburg MD, 20899 (2000), <https://doi.org/10.18434/T4T88K>.
- [38] W. Eberhardt et al., *Phys. Rev. Lett.* 64 (7) (1990) 780.
- [39] Y.T. Kim et al., *Angew. Chem.-Int. Edit.* 45 (3) (2006) 407.
- [40] O.V. Yazyev, A. Pasquarello, *Phys. Rev. B* 82 (4) (2010) 045407.
- [41] J.M. Hodges et al., *J. Am. Chem. Soc.* 137 (49) (2015) 15493.
- [42] Y. Ridelman et al., *Small* 8 (5) (2012) 654.
- [43] Y. Sun et al., *Nat. Chem.* (2020) 1.
- [44] X. Li et al., *Sustain. Energy Fuels* 4 (8) (2020) 3884.
- [45] T. Liu et al., *Adv. Energy Mater.* 7 (15) (2017) 1700020.
- [46] S. Xu et al., *J. Mater. Chem. A* 8 (38) (2020) 19729.
- [47] L. Zhang et al., *Small Struct.* 2 (2) (2021) 2000048.
- [48] D. Liu et al., *Nat. Energy* 4 (6) (2019) 512.
- [49] J. Zhang et al., *Nat. Catal.* 1 (12) (2018) 985.
- [50] J.N. Tiwari et al., *Nat. Energy* 3 (9) (2018) 773.
- [51] K. Jiang et al., *Nat. Commun.* 10 (1) (2019) 1.
- [52] N. Cheng et al., *Nat. Commun.* (2016) 7.
- [53] Q. Liu, Z. Zhang, *Catal. Sci. Technol.* 9 (18) (2019) 4821.
- [54] N.C. Cheng et al., *Nat. Commun.* 7 (2016) 9.
- [55] H.H. Wei et al., *Nat. Commun.* 8 (2017) 8.
- [56] J. Mahmood et al., *Nat. Nanotechnol.* 12 (5) (2017) 441.
- [57] B.E. Conway, B.V. Tilak, *Electrochim. Acta* 47 (22–23) (2002) 3571.
- [58] S. Trasatti, *J. Electroanal. Chem.* 39 (1) (1972) 163.
- [59] H. Liu et al., *Sci. Rep.* 4 (2014) 7.
- [60] N. Tushima et al., *J. Phys. Chem. B* 109 (34) (2005) 16326.
- [61] Y. Zhang et al., *Nano Res.* 12 (4) (2019) 919.
- [62] Z. Nie et al., *Nat. Nanotechnol.* 5 (1) (2010) 15.